Annual modulation of non-volcanic tremor in northern Cascadia

Fred F. Pollitz,[1] Aaron Wech,[2] Honn Kao,[3] and Roland Bürgmann[4]

[1]   Two catalogs of episodic tremor events in northern Cascadia, one from 2006 to 2012 and the other from 1997 to 2011, reveal two systematic patterns of tremor occurrence in southern Vancouver Island: (1) most individual events tend to occur in the third quarter of the year; (2) the number of events in prolonged episodes (i.e., episodic tremor and slip events), which generally propagate to Vancouver Island from elsewhere along the Cascadia subduction zone, is inversely correlated with the amount of precipitation that occurred in the preceding 2 months. We rationalize these patterns as the product of hydrologic loading of the crust of southern Vancouver Island and the surrounding continental region, superimposed with annual variations from oceanic tidal loading. Loading of the Vancouver Island crust in the winter (when the land surface receives ample precipitation) and unloading in the summer tends to inhibit and enhance downdip shear stress, respectively. Quantitatively, for an annually variable surface load, the predicted stress perturbation depends on mantle viscoelastic rheology. A mechanical model of downdip shear stress on the transition zone beneath Vancouver Island—driven predominantly by the annual hydrologic cycle—is consistent with the 1997–2012 tremor observations, with peak-to-peak downdip shear stress of about 0.4 kPa. This seasonal dependence of tremor occurrence appears to be restricted to southern Vancouver Island because of its unique situation as an elongated narrow-width land mass surrounded by ocean, which permits seasonal perturbations in shear stress at depth.

1. Introduction

[2] Episodic tremor events are commonly observed at the Cascadia subduction zone (Figure 1). They usually occur as part of prolonged episodic tremor and slip (ETS) events at depth $\gtrsim$ 25 km, corresponding to the transition zone below the seismogenic (locked) portion of the megathrust [*Dragert et al.*, 2001; *Rogers and Dragert*, 2003]. Where they occur may correspond to a partially locked section of the subduction zone as suggested by residual slip deficit inferred from geodetic slip models of ETS events and interseismic strain accumulation [*Chapman and Melbourne*, 2009]. Seismic tremor episodes are well correlated with geodet-

ically measured motions at Earth's surface [*Miller et al.*, 2002; *Rogers and Dragert*, 2003], suggesting that they are associated with slip on the subduction interface. This interpretation is supported by the locations and focal mechanisms of low-frequency earthquakes beneath southern Vancouver Island [*Bostock et al.*, 2012]. Tidal stresses are known to influence the occurrence of both non-volcanic tremor (NVT) [*Rubinstein et al.*, 2008] and slow slip [*Hawthorne and Rubin*, 2010]. During a slow-slip event, which may have a duration from days to weeks [*Aguiar et al.*, 2009; *McCausland et al.*, 2005], the occurrence of slow slip is well correlated with the semidiurnal tide [*Hawthorne and Rubin*, 2010]. The low shear stress changes associated with the semidiurnal tide (on the order of 1 kPa) suggests that tremor events occur in a regime where the resisting normal stress is near zero, i.e., the effective coefficient of friction is near zero. This is consistent with the inferences of low friction based on sensitivity to dynamic stress [*Rubinstein et al.*, 2007] and high pore fluid pressure in the transition zone based on seismic studies [*Audet et al.*, 2009, 2010].

[3] Tremor and slow slip in northern Cascadia tends to occur with a near-14 month periodicity [e.g., *Miller et al.*, 2002; *Brudzinski and Allen*, 2007; *Kao et al.*, 2009; *Wech et al.*, 2009]. Inter-event times of major ETS are different for central and southern Cascadia [e.g., *Gomberg and the Cascadia 2007 and Beyond Working Group*, 2010]. Over the period 1997 to 2004, tremor occurrence is well correlated

---

[1]U.S. Geological Survey, Menlo Park, California, USA.
[2]Alaska Volcano Observatory, U.S. Geological Survey, Anchorage, Alaska, USA.
[3]Geological Survey of Canada, Natural Resources Canada, Pacific Geoscience Centre, Sidney, British Columbia, Canada.
[4]Department of Earth and Planetary Science, UC Berkeley, California, USA.

Corresponding author: F. F. Pollitz, U.S. Geological Survey, 345 Middlefield Rd., MS 977, Menlo Park, CA 94025, USA. (fpollitz@usgs.gov)
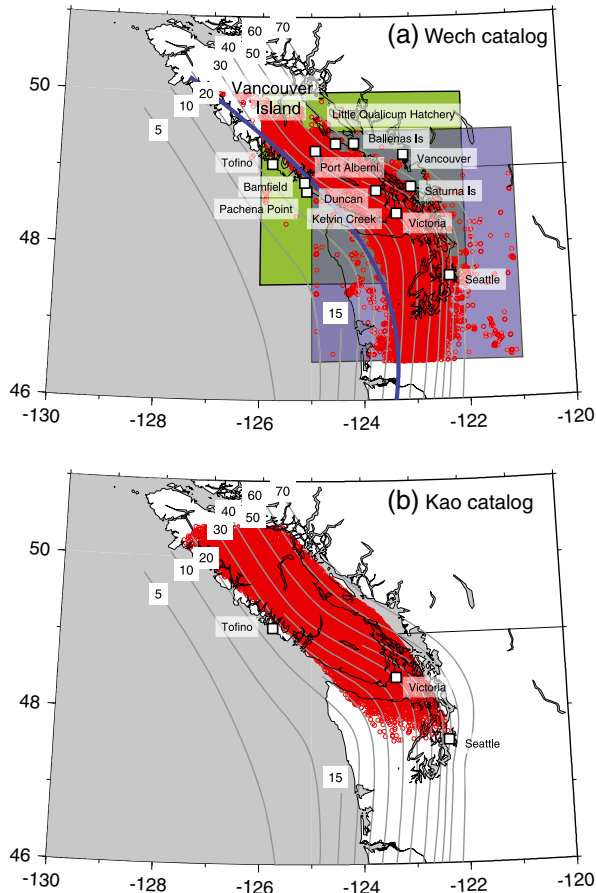
Figure 1. (a) Epicenters of NVT events using the 2006–2012 Wech catalog [*Wech*, 2010]. The thick blue line indicates the upward limit of downdip distance (defined such that 98% of tremor events at a given latitude occur east of this line). Green and blue rectangular regions define the BC and NW regions. (b) Epicenters of NVT events using the 1997–2011 Kao catalog [*Kao et al.*, 2009]. Gray lines are contours of *McCrory et al.* [2006] in kilometer depth to the top of the subducting Juan de Fuca slab.

with peak shear stress generated by the pole tide, which is related to the Chandler wobble with a ∼ 14 month periodicity [*Shen et al.*, 2005]. However, a 28 year-long ETS catalog (Herb Dragert, pers. comm.) reveals that before 1997, ETS epoch times retain almost the same 14 month periodicity but are generally out of phase with the peak pole-tide stress. The longer catalog thus suggests that the correlation between the two in the 1997–2004 period is largely serendipitous and that the pole tide is not the dominant physical driving force.

[4] *Lowry* [2006] proposed that the annual hydrological cycle caused seasonal stress perturbations that modulated episodic slip events in Guerrero, Mexico based on 4 years of GPS observations. However, this observation has been questioned by *Vergnolle et al.* [2010] using an 11 year-long catalog. *Heki and Kataoka* [2008] found 6 month repeat cycles for slow-slip events in Ryuko, but no convincing correlation with seasons, the slip events tending not to occur in any particular months.

[5] Observations by the Gravity Recovery and Climate Experiment (GRACE) satellite and the Global Land Data Assimilation System (GLDAS) indicate relatively large fluctuations in equivalent water mass around Vancouver Island over the year, on the order of ±10 cm, one of the largest such annual fluctuations outside Earth's tropical regions. This is consistent with a large amount of observed annual precipitation and monthly variations on Vancouver Island (Figure 2). We shall show that the magnitude of stress perturbations associated with the annual cycle are of the same order as that associated with the semidiurnal cycle, and they depend substantially on the viscoelastic structure of Earth's mantle. The annual hydrologic cycle is known to have a tangible effect on seismicity in the Himalaya of Nepal [*Bollinger et al.*, 2007; *Bettinelli et al.*, 2008], with associated driving stresses on the order of 1 kPa. Similar seasonal forcing related to snow accumulation is correlated with interplate seismicity off Japan [*Heki*, 2001] and along the San Andreas fault in Central California [*Christiansen et al.*, 2007] with driving stresses up to several kilopascal. For a suitable mantle viscoelastic structure, the annual stress perturbations that we estimate for northern Cascadia are of magnitude 0.4 kPa.

[6] In this paper we use two detailed catalogs of tremor. The first catalog ("Wech Catalog") is an update of that presented by *Wech et al.* [2009] and is available online [*Wech*, 2010]. It includes both ETS and inter-ETS events along the Cascadia margin from 39°N to 50°N from early 2006 to early 2012. The second catalog ("Kao catalog") is an update of that presented by *Kao et al.* [2009] and covers the northern part of the Cascadia margin (i.e., Vancouver Island) from 1997 through 2011. These catalogs provide an opportunity to investigate the possible influence of the annual hydrologic cycle in Cascadia using a long and rich record of tremor. We test a model of annual hydrologic stress changes through a combination of forward modeling and detailed observations of NVT in northern Cascadia over the past several years.
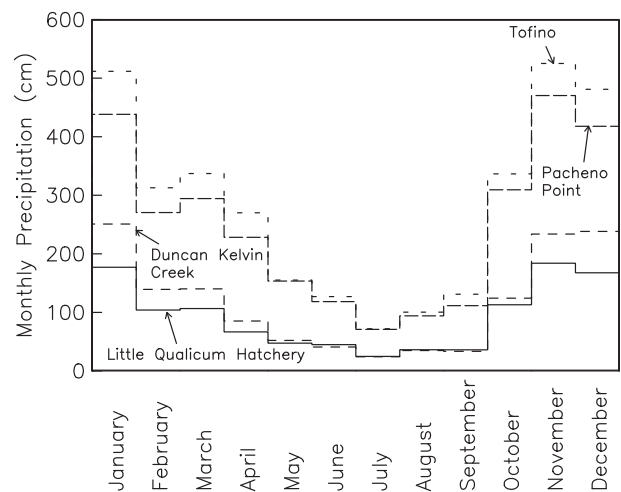

Figure 2. Average monthly precipitation from 1987–2007 at selected locations on Vancouver Island. Site locations are indicated in Figure 1. Data are from National Climate Data and Information Archive (http://www.climate.weatheroffice.gc.ca).
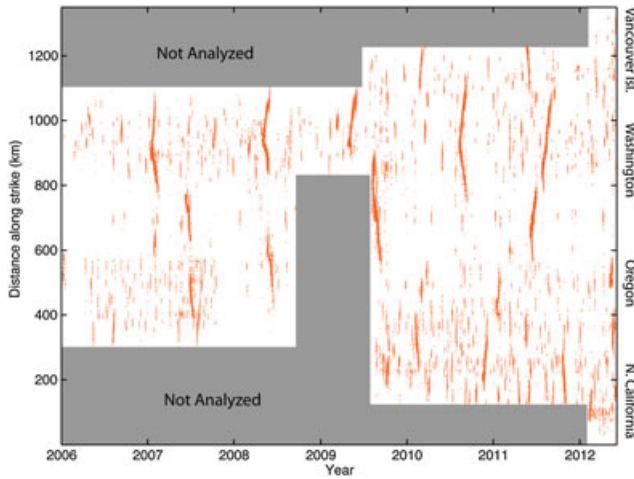
2

Figure 3. Occurrence times and distance along strike of NVT events using the 2006–2012 Wech catalog.

2. Six Year and Fourteen Year Tremor Catalogs in Northern Cascadia

[7] An NVT-detection algorithm described by *Wech and Creager* [2008] enables the identification of numerous small tremor events over the period 2006–2012 between the latitudes of 39.00 and 50.00°N. The northern portion of this catalog is shown in Figure 1a in map view, and in Figure 3 in terms of the along-strike distance to each tremor event. This catalog is a composite of two subcatalogs determined with respective sets of seismic stations in British Columbia, Canada and the Pacific Northwest, United States (Figure S1a, in the supporting information). In particular, two subsets of the catalog—those NVT epicenters lying within the British Columbia (BC) and Pacific Northwest
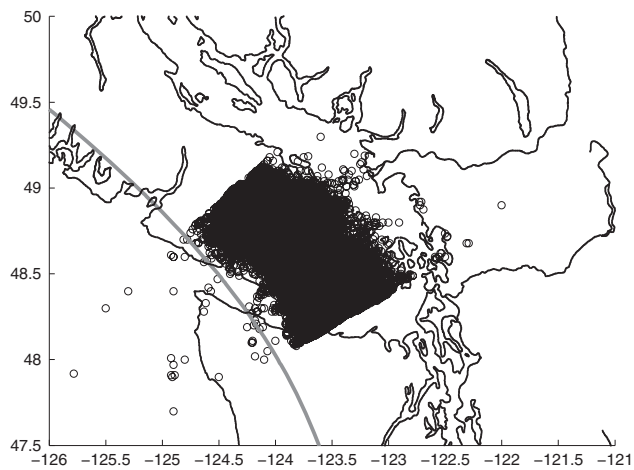

Figure 4. Epicenters of NVT events using the combined BC and NW portions of the Wech catalog restricted to along-strike distance between 1000 and 1100 km. The thick gray line indicates the upward limit of downdip distance (defined such that 98% of tremor events at a given latitude occur east of this line).
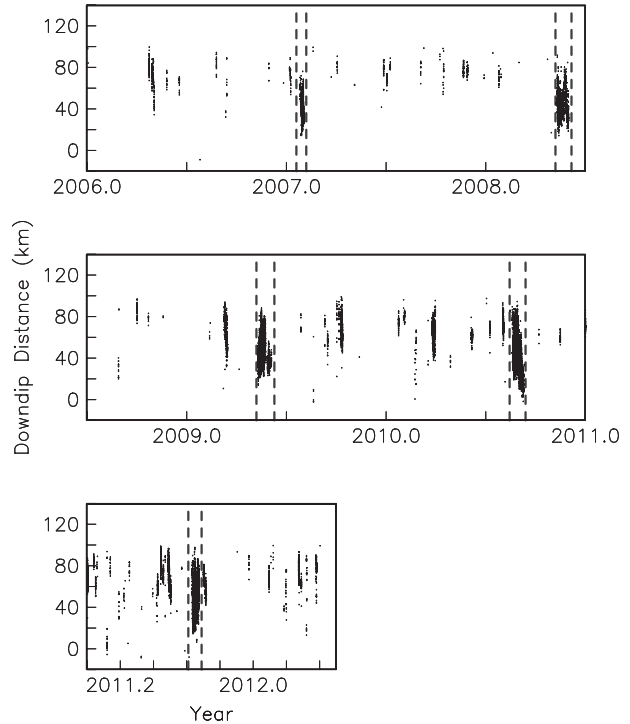

Figure 5. Occurrence times and downdip distance of NVT events using the combined BC and NW portions of the Wech catalog restricted to along-strike distance between 1000 and 1100 km. Dashed lines bracket the times of major ETS.

(NW) regions shown in Figure 1a—have been determined with processing of these separate sets of seismic stations.

[8] We delineate the southern Vancouver Island region with the criterion that along-strike distance is between 1000 and 1100 km, as measured from the southernmost part of the convergent plate boundary off Northern California. The BC and NW region catalogs have been combined and edited according to a simple space-time criterion designed to remove redundant entries arising from their separate processing. The resulting combined BC and NW catalogs restricted to southern Vancouver Island are shown in terms of along-strike distance in Figure 4 and in terms of the downdip distance to each event in Figure 5. Within the southern Vancouver Island region, there are altogether 18,220 tremor events in 6 years. Because the tremor epicenters are typically better determined than their depth, their epicenters are projected to depth by means of a model of slab depth [e.g., *McCrory et al.*, 2006]. A reference distance of zero is that downdip distance at which 2% of the events along binned coast-parallel profiles are located at shallower depth (Figure 1a), and this reference line is generally a smoothly varying function of distance parallel to the coast. In southern Vancouver Island, this reference line closely follows the 30 km depth contour of *McCrory et al.* [2006].

[9] *Kao et al.* [2009] use a tremor detection method which uses a grid search to maximize the "brightness" of a hypothetical event using a stack of observed seismograms windowed to expected arrival times of events at trial locations and origin times. With a brightness threshold, this "source
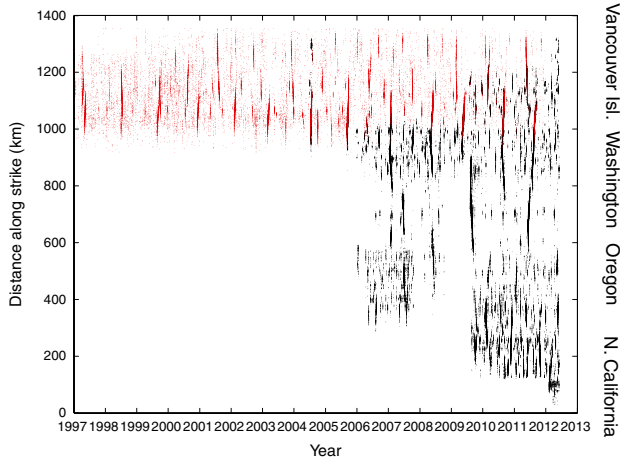
Figure 6. Occurrence times and distance along strike of NVT events using the 1997–2011 Kao catalog, shown with red dots. Superposed with black dots are the tremor events using the Wech catalog from 2006–2012 (redundant with Figure 3).

scanning algorithm" yields a catalog of tremor times and locations. The resulting catalog from 1997–2011 is shown in Figure 1b in map view, in terms of along-strike distance in Figure 6, and in terms of the downdip distance to each event in Figure 7. Within the southern Vancouver Island region, there are altogether 19,466 tremor events in 14 years. Since the method has been applied to a set of stations on Vancouver Island, the Kao catalog is restricted to along-strike-distances of $\gtrsim$ 1000 km. It overlaps substantially with the Wech catalog in the 1000 to 1100 km distance range, where the locations of tremor events agree quite well (Figure 6).

[10] Many of the small events comprise the large ETS every $\sim$ 14 months, but, as first noted by *Kao et al.* [2009] and *Wech et al.* [2009], numerous inter-ETS events are also detected, and these tend to occur in relatively small clusters. The inter-ETS events are evident in both the Wech and Kao catalogs (Figures 3 and 6), which demonstrate that these smaller events occur along the entire length of the Cascadia subduction zone. Inspection of tremor histories in Figures 5 and 7 suggests that inter-ETS tend to occur more frequently in the latter half of an inter-ETS period.

[11] Tremor events tend to occur in the third quarter of the year as seen through monthly histograms of tremor counts using various catalogs (Figure 8). The catalogs shown in Figure 8 sample different parts of the Cascadia margin, e.g., the BC catalog covers the latitude range 47.5°N to 50°N (Figure 3) and the Kao catalog is restricted to Vancouver Island and northernmost Washington (Figure 6), whereas the NW catalog covers much of Washington. The event counts in the figure are edited to a common range of 1000 to 1100 km along-strike distance, i.e., southern Vancouver Island, but different distributions of employed seismic stations will result in different resolutions of tremor. The most obvious differences in the event histograms among these catalogs are in the month of May: the peak in the NW catalog is from the May 2008 ETS in Washington (Figure 3), whereas the peak in the Kao catalog is from ETS in May

2008 (in Washington) and May 2009 in southern Vancouver Island (Figure 6).

[12] Figure 9 shows histograms of the number of NVT events by quarter of the year in which they occurred for both the combined (BC + NW) Wech catalog and Kao catalog, respectively. Separate histograms are shown for all events or only deeper (> 40 km depth) events. The figure confirms that both catalogs have a pronounced peak in the third quarter, regardless of the restriction on depth of tremor. The two catalogs are based on different methodologies and distributions of seismic stations, so that their common temporal pattern suggests a robust seasonal pattern in NVT occurrence in northern Cascadia.

[13] We test the statistical significance of the third-quarter peak using the Kao catalog since it spans a longer time interval and has many more sub-events. To do this, we construct a set of random catalogs beginning with the Kao catalog from which all events of along-strike distance 1000 to 1100 km are extracted. We recognize 13 ETS events within this catalog (e.g., Figure 6). In one realization, we assign a random time (an ETS "summary time") to each ETS using the uniform distribution between the times of 1997.0 and 2012.0. We then assign a random time to each event in the Kao catalog by assigning the appropriate ETS summary time to each event that occurred within a real ETS cluster
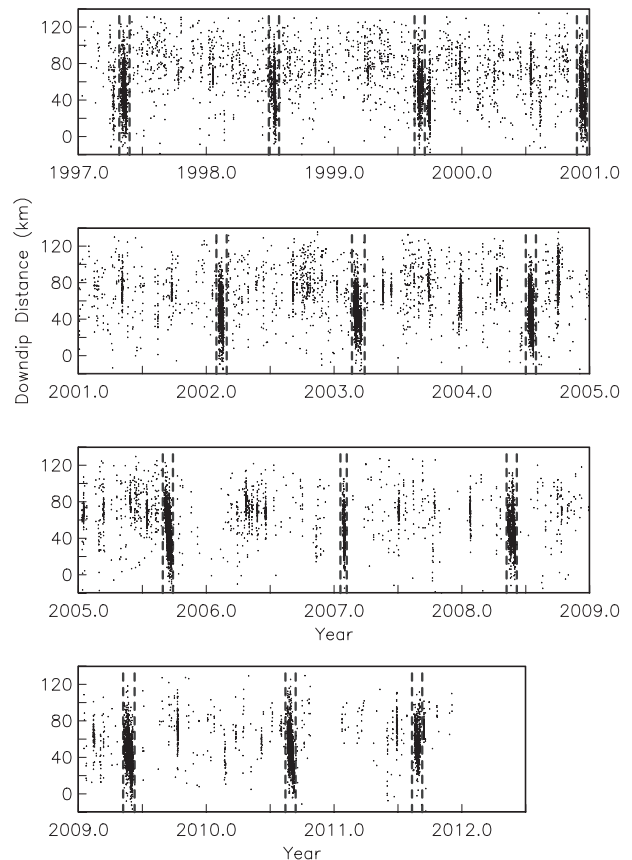

Figure 7. Occurrence times and downdip distance of NVT events using the Kao catalog restricted to along-strike distance between 1000 and 1100 km. Dashed lines bracket the times of major ETS.
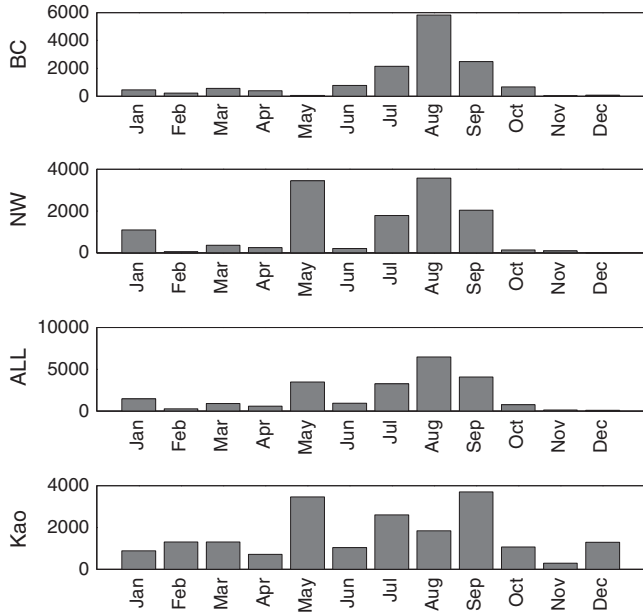
Figure 8. Histograms of NVT occurrence binned by month using the Wech BC catalog (Figure 1a), Wech NW catalog (Figure 1a), combined Wech BC+NW catalog (labelled ALL) (Figures 3–5), and the Kao catalog (Figure 6). All catalogs are restricted to along-strike distance of 1000 to 1100 km.

(as delineated in Figure 7), otherwise (for inter-ETS events) a random time between 1997.0 and 2012.0. We perform 4000 realizations and evaluate the fraction of events f occurring in the third quarter in each. This yields a synthetic probability distribution of f using random catalogs that preserve the existence of 13 ETS clusters with the same number of events per cluster as is observed. The resulting histogram in Figure 10 shows that the observed f-value of 0.416 is significant at > 95%. The results are similar when events are restricted to > 40 km depth.

[14] We find a striking anti-correlation between ETS-event size and the precipitation in southern Vancouver Island in the 2 months leading up to the ETS for both the Wech catalog spanning 5 years and the Kao catalog spanning 15 years (Figure 11). In the Wech catalog, the January 2007 and August 2010 ETS are associated with the smallest and largest numbers of sub-events, respectively, with correspondingly high and low precipitation; in the Kao catalog, the January 2007 and August 2005 ETS are associated with the smallest and largest number of sub-events, respectively, with correspondingly high and low precipitation. All ETS during the 2006–2011 period propagated northward to Vancouver Island [*Wech et al.*, 2009] from further south. The identified pattern suggests that the degree of northward propagation is controlled by the hydrologic load in place at the time of the episode. This factor could enhance (or inhibit) the tendency of ruptures to reverse course during a prolonged tremor episode, when already ruptured patches are thought to be more susceptible to further rupture during the short term [*Houston et al.*, 2011].

[15] We hypothesize that the hydrological cycle adds an annual contribution to the stresses on the transition zone

of the northern Cascadia slab interface. The maximum/minimum water loads in this region are achieved in mid-winter and mid-summer, respectively. As will be clear from the analysis in the next section, the effect of such loads on stress in the transition zone will be greatest during the unloading portion.

[16] In the following sections, we construct a theoretical model of the response of a viscoelastic Earth to a periodic forcing, then apply it to annual mass changes detected by GRACE, GLDAS, and absolute gravity.
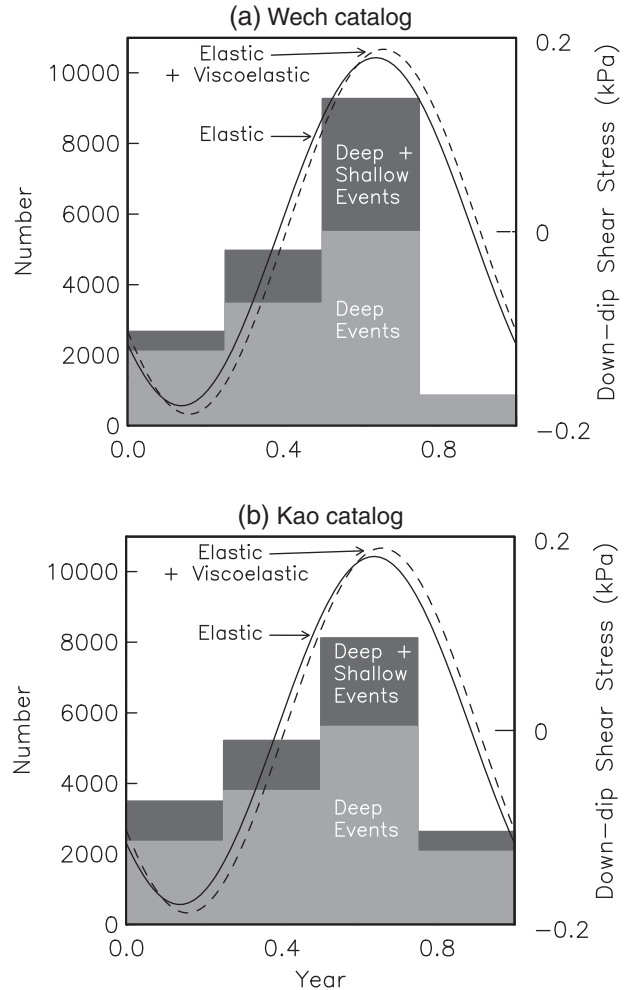

Figure 9. Histograms of NVT occurrence binned by quarter of the year using the combined (BC + NW) Wech catalog (black symbols in Figures 5 and 6) and the Kao catalog (red symbols in Figure 6). Values from 0 to 1 on the *x*-axis span an entire year. Results are shown for both combined deep and shallow events (dark shading) and deep events alone (light shading), corresponding to events with downdip distance greater than 45 km (corresponding to depth $\gtrsim$ 40 km). Superimposed is the time-dependent downdip shear stress at 45 km depth based on the model of annual hydrologic loading described in section 6. Both the elastic and summed elastic and viscoelastic components model predictions (equation (7)) are shown.
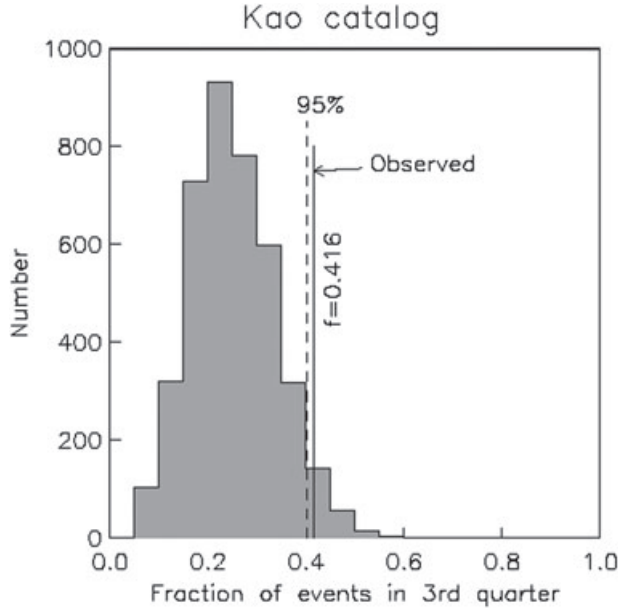
Figure 10. Histograms of fraction of events occurring in the third quarter f resulting from 4000 realizations of random catalogs derived from the Kao catalog. The observed fraction $f = 0.416$ is significant at the 96.3% level.

3. Oscillations of a Spherically Layered Viscoelastic Earth

[17] We consider the time-dependent crustal stress field resulting from a force distributed over a volume (or surface) that acts sinusoidally in time. We work initially in the Laplace transform domain. The Laplace transform of a function $f(t)$ with independent variable s is

$$\tilde{f}(s) = L[f(t)] = \int_0^\infty f(t) \exp(-st)\, dt \tag{1}$$

Following the semi-analytic treatments of static displacements and post-earthquake relaxation on a spherically stratified Earth model [*Pollitz*, 1996, 1997, 2003], let time-dependent point forces $\mathbf{f}(\mathbf{r}_0, t)$ be distributed over a source volume V. We represent the Laplace-transformed displacement $\tilde{\mathbf{u}}(\mathbf{r}, s)$ at position $\mathbf{r}$ resulting from the distributed force as

$$\tilde{\mathbf{u}}(\mathbf{r}, s) = \int_{\mathbf{r}_0 \in V} \sum_{i=1}^{3} \sum_{j} \left[\mathbf{A_{ij}}(\mathbf{r}; \mathbf{r}_0) + \mathbf{B_{ij}}(\mathbf{r}; \mathbf{r}_0)\, \Psi_j(s) \right] \tilde{f}_i(\mathbf{r}_0, s)\, d^3\mathbf{r}_0 \tag{2}$$

where the $\{\mathbf{A_{ij}}\}$ and $\{\mathbf{B_{ij}}\}$ are vector Green's functions for the static and viscoelastic relaxation deformation fields (which depend on the source-observation point angular distance, source and observation point radius), with j denoting static (or viscoelastic) mode index, and

$$\Psi_j(s) = \frac{1}{s + s_j} \tag{3}$$

where s_j is the inverse characteristic relaxation time of viscoelastic mode j [*Pollitz*, 1997].

[18] For forcing which behaves as a step function in time, $\tilde{f}_i(\mathbf{r}_0, s) = F_i(\mathbf{r}_0)/s$, and hence

$$\mathbf{u}(\mathbf{r}, t) = \int_{\mathbf{r}_0 \in V} \sum_{i=1}^{3} \sum_{j} \left[\mathbf{A_{ij}}(\mathbf{r}; \mathbf{r}_0) + \mathbf{B_{ij}}(\mathbf{r}; \mathbf{r}_0) \frac{1 - \exp(-s_j t)}{s_j} \right]$$
$$\cdot H(t)\, F_i(\mathbf{r}_0)\, d^3\mathbf{r}_0 \tag{4}$$

where $H(t)$ is the Heaviside step function.

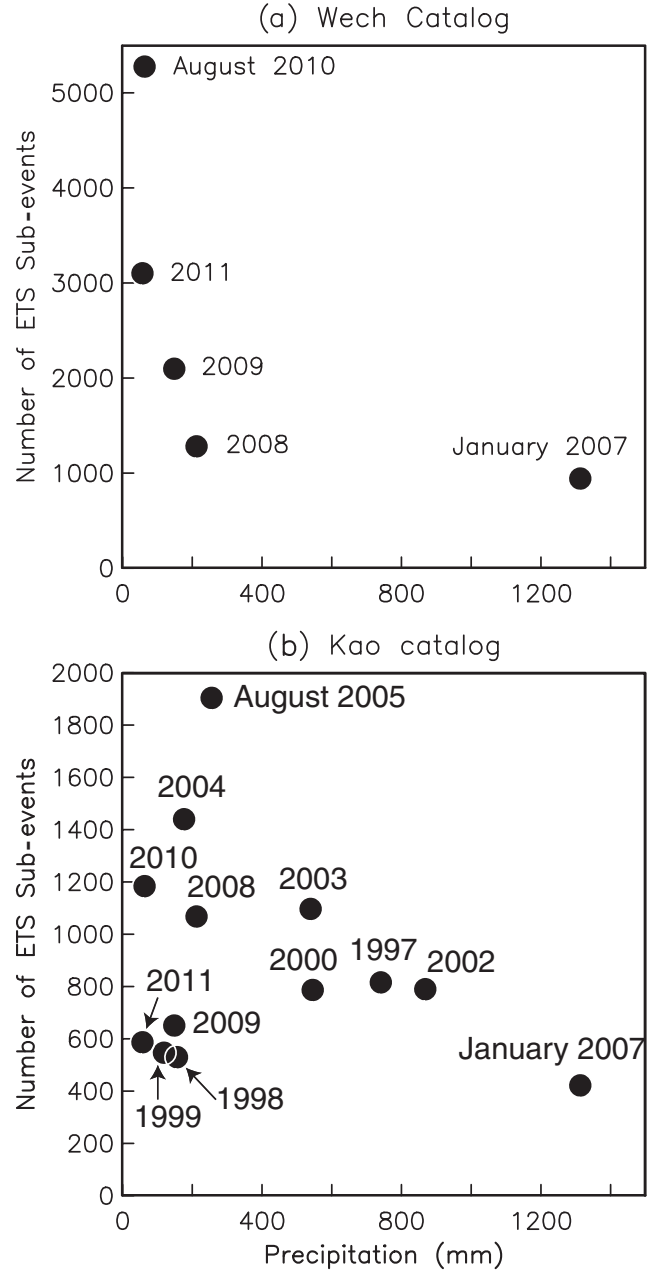**Figure 11.** Number of ETS sub-events within the windows shown in (a) Figure 5 for the Wech catalog or (b) Figure 7 for the Kao catalog as a function of the total precipitation that occurred in the month of the considered event and the preceding month (e.g., December 2006 and January 2007 for the January 2007 ETS). Precipitation data are from National Climate Data and Information Archive (http://www.climate.weatheroffice.gc.ca).
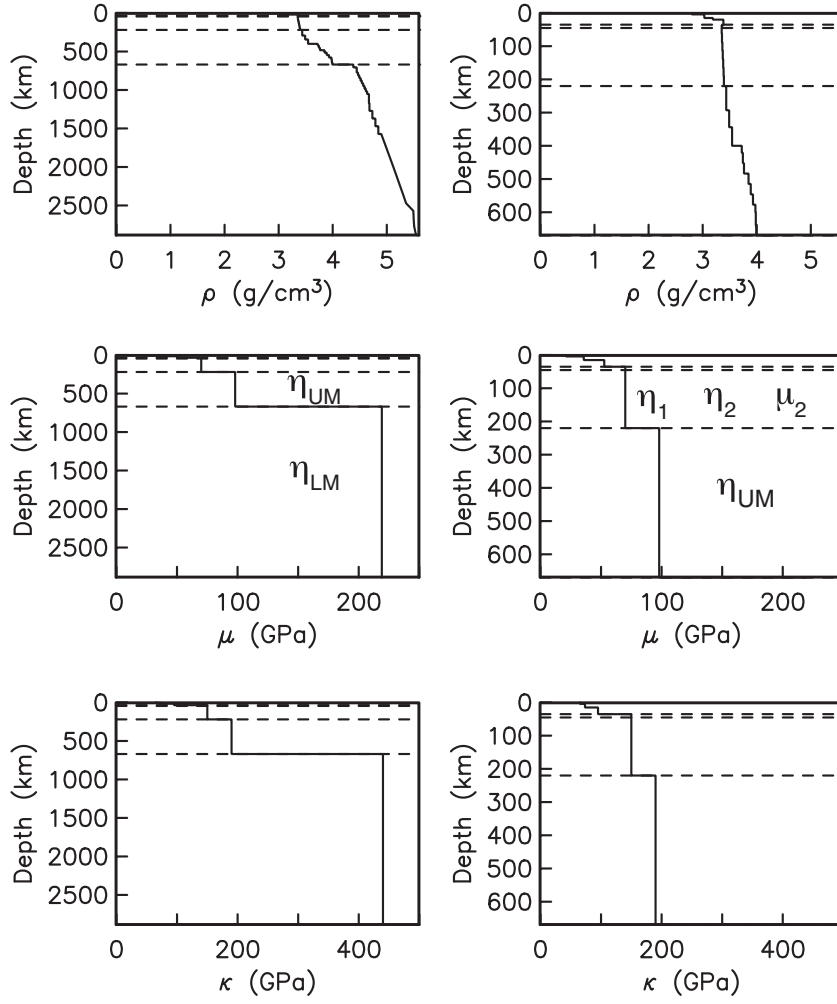
Figure 12. Elastic structure assumed in this study, shown by the discontinuous black curves in each panel. Discontinuities are present at depths 35, 45, 220, 670, and 2891 km. As indicated in the middle panels, the steady state and transient viscosity and transient shear modulus in the asthenosphere are η_1, η_2, and μ_2, respectively. The upper mantle and lower mantle viscosity are η_{UM} and η_{LM}, respectively. Viscosity values are provided in section 4.1.

[19] For forcing which behaves as a harmonic oscillator with angular frequency ω,

$$f_i(\mathbf{r}_0, t) = F_i(\mathbf{r}_0) \cos \omega t \, H(t)$$

$$\tilde{f}_i(\mathbf{r}_0, s) = F_i(\mathbf{r}_0) \left(\frac{s}{s^2 + \omega^2} \right) \tag{5}$$

Substitution of equation (5) into equation (1) and evaluation of the inverse Laplace transform yields

$$\mathbf{u}(\mathbf{r}, t) = \int_{\mathbf{r}_0 \in V} \sum_{i=1}^{3} \sum_{j} \left[\mathbf{A_{ij}}(\mathbf{r}; \mathbf{r}_0) \cos \omega t + \mathbf{B_{ij}}(\mathbf{r}; \mathbf{r}_0) \right.$$

$$\left. \times \frac{1}{s_j^2 + \omega^2} (\omega \, \sin \omega t + s_j \, \cos \omega t) \right] H(t) \, F_i(\mathbf{r}_0) \, d^3\mathbf{r}_0$$

$$- \int_{\mathbf{r}_0 \in V} \sum_{i=1}^{3} \sum_{j} \mathbf{B_{ij}}(\mathbf{r}; \mathbf{r}_0) \frac{s_j}{s_j^2 + \omega^2} \exp(-s_j t) H(t) \, F_i(\mathbf{r}_0) \, d^3\mathbf{r}_0 \tag{6}$$

For small ω, this solution reduces to that of the step-function forcing (equation (4)). At time much greater than any characteristic relaxation time ($t \gg \max\{1/s_j\}$), the second integral becomes vanishingly small, and thus at sufficiently long time after the initiation of forcing

$$\mathbf{u}(\mathbf{r}, t) = \int_{\mathbf{r}_0 \in V} \sum_{i=1}^{3} \sum_{j} \left[\mathbf{A_{ij}}(\mathbf{r}; \mathbf{r}_0) \cos \omega t + \mathbf{B_{ij}}(\mathbf{r}; \mathbf{r}_0) \right]$$

$$\left[\times \frac{1}{s_j^2 + \omega^2} (\omega \, \sin \omega t + s_j \, \cos \omega t) \right] H(t) \, F_i(\mathbf{r}_0) \, d^3\mathbf{r}_0 \tag{7}$$

We shall refer to the $\mathbf{A_{ij}}$ and $\mathbf{B_{ij}}$ terms of equation (7) as the "elastic" and "viscous" components of the oscillating solution. For large ω, the factors multiplying the viscous part of the solution tend to zero, and the resulting solution behaves as that of the equivalent elastic model. For large viscosity, all s_j tend to zero, and because of the normalization of the viscoelastic Green's functions, the $\mathbf{B_{ij}}$ tend to zero, so that

the resulting solution again behaves as that of the equivalent elastic model.

[20] For a homogeneous viscoelastic material subjected to harmonic forcing, there is both amplification and a phase shift of the stress response relative to the response on the equivalent elastic material (Appendix A). The same is true on a layered viscoelastic Earth model, but the response is more complicated because of the presence of an elastic uppermost layer and other layering. Equation (7) may be rewritten as

$$\mathbf{u}(\mathbf{r}, t) = \int_{\mathbf{r}_0 \in V} \sum_{i=1}^{3} \sum_{j} \left[\mathbf{A_{ij}}(\mathbf{r}; \mathbf{r}_0) + \mathbf{B_{ij}}(\mathbf{r}; \mathbf{r}_0) \frac{s_j}{s_j^2 + \omega^2} \right]$$
$$\cdot F_i(\mathbf{r}_0) \, d^3\mathbf{r}_0 \, \cos \omega t \, H(t)$$
$$+ \int_{\mathbf{r}_0 \in V} \sum_{i=1}^{3} \sum_{j} \mathbf{B_{ij}}(\mathbf{r}; \mathbf{r}_0) \frac{\omega}{s_j^2 + \omega^2} F_i(\mathbf{r}_0) \, d^3\mathbf{r}_0 \, \sin \omega t \, H(t)$$
(8)

Comparing the $\cos \omega t$ and $\sin \omega$ terms of equation (8), it is clear that the solution may be written in the form $\mathbf{u} = C \cos(\omega t + \xi) H(t)$, where both C and ξ depend on the Green's functions of all static and viscoelastic modes in a manner which depends on the details of the viscoelastic structure. As remarked above, C approaches that of the equivalent elastic model and ξ approaches zero in the limit of large ω or viscosity.

4. Example

4.1. Viscoelastic Structure

[21] Consider the viscoelastic structure specified in Figure 12, which is the *Pollitz et al.* [2006] biviscous viscoelastic structure (used to model post-earthquake relaxation following the 2004 Sumatra-Andaman earthquake) modified to have a crustal thickness of 35 km and an elastic plate thickness of 45 km. Thus, the crust and upper 10 km of the mantle behave elastically. Following the definitions of transient and steady-state viscosities given in Figure 1 and equation (5) of *Pollitz* [2003], this model has transient and steady-state viscosities of $\eta_2 = 5 \times 10^{17}$ Pa s and $\eta_1 = 10^{19}$ Pa s, respectively, in the asthenosphere, transient shear modulus $\mu_2 = 70$ GPa (which equals the steady state shear modulus), upper mantle Maxwellian viscosity $\eta_{UM} = 10^{20}$ Pa s and lower mantle Maxwellian viscosity $\eta_{LM} = 10^{21}$ Pa s. This model (or models with similar parameter values) explains time-dependent deformation following the 2004 Sumatra earthquake and other great subduction-zone earthquakes when viscoelastic relaxation is modeled jointly with afterslip [e.g., *Panet et al.*, 2010; *Hu and Wang*, 2012; *Wang et al.*, 2012]. The steady state viscosity is consistent with the range $\eta_1 = 3 \times 10^{18}$ Pa s to 4×10^{19} Pa s inferred by *James et al.* [2009] on the basis of postglacial rebound modeling. We prefer the biviscous model because it appears more accurate for explaining transient deformation that is sensitive to shorter timescale relaxation [e.g., *Pollitz et al.*, 2006; *Wang et al.*, 2012].

[22] Viscoelastic mode dispersion is represented in Figure 13 in terms of the viscoelastic decay times $2\pi\tau = 2\pi/s_j$ for the sets $\{s_j\}$ determined for the spheroidal and toroidal motion cases separately. Because of the low-viscosity Kelvin component of the asthenosphere rheology,
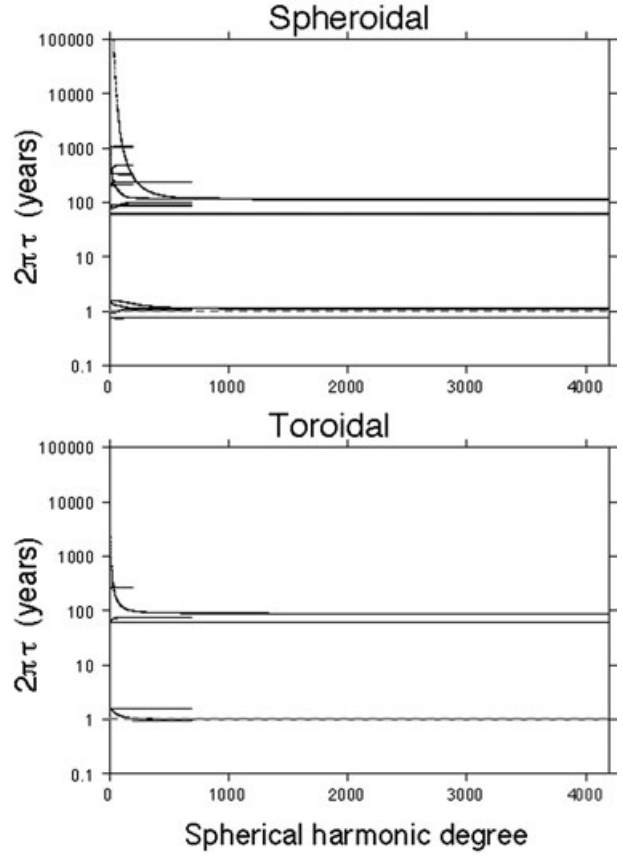

Figure 13. Scaled characteristic decay times $2\pi\tau = 2\pi/s_j$ for the sets of $\{s_j\}$ determined for spheroidal and toroidal motion cases. Mode branches truncated at $l = 191$ or $l = 631$ correspond to viscoelastic relaxation confined almost entirely to the regions deeper than the 660 or 220 km discontinuities, respectively. Dashed gray line indicates the 1 year annual cycle.

several decay times are on the order of 1 year (marked by red lines in Figure 13) and thus are expected to contribute significantly to the cyclic deformation driven by the annual hydrological cycle. Although they do not contribute to the displacement field generated by a vertical force, the toroidal mode dispersion is shown for completeness.

4.2. Continuous Load

[23] A vertical force with annual periodicity ($\omega = 2\pi/\text{yr}$) is imposed on Earth's surface equivalent to the removal of 10 cm water load over an area of radius 3.5 geocentric degrees centered on 51.2°N, 121.5°W. In Figure 14, the displacement response at 36 km depth on the viscoelastic Earth is represented by the three separate terms in equation (7): the elastic $\cos \omega t$, viscous $\cos \omega t$, and viscous $\sin \omega t$ terms. The displacement pattern of the elastic $\cos \omega t$ term (Figure 14a) is consistent with upward motion of a broad area surrounding the water load, with corresponding horizontal displacements away from the center of the load. The displacement pattern of the viscous $\cos \omega t$ term (Figure 14b) is consistent with relaxation of the asthenosphere beneath and surrounding the load. This relaxation permits additional uplift in the immediate area of mass removal. Since this is accompa-
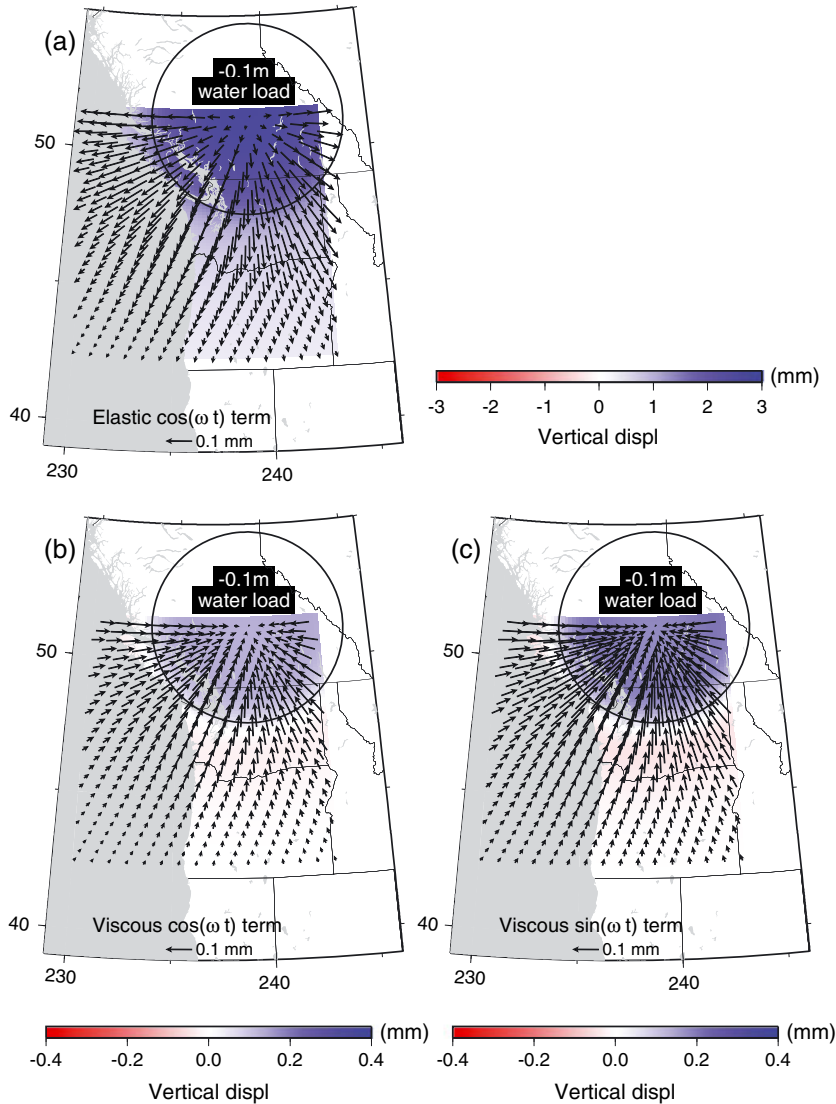
Figure 14. (a) Elastic $\cos \omega t$, (b) viscous $\cos \omega t$, and (c) viscous $\sin \omega t$ components of the viscoelastic response for annual loading of Earth's surface with an equivalent 10 cm water load over the indicated region. Horizontal and vertical displacements are evaluated at 36 km depth.

nied by motion of fluid mantle toward the center of the load (to fill in the void created by the additional uplift), attached crust is dragged by the viscous mantle flow toward the center of the load—in the opposite sense of the elastic horizontal displacement. The mantle flow field also removes mass from the mantle outside the load area, resulting in subsidence of that area. The vertical and horizontal displacement patterns of the viscous $\sin \omega t$ term (Figure 14c) are about 50% larger than those associated with the viscous $\cos \omega t$ term, so that the flow-induced deformation described above has a $\cos(\omega t - \xi)$ time dependence with $\xi \approx 1.0$ rad, i.e., the viscous component lags about 1.0 rad in phase behind the elastic component.

[24] The corresponding downdip shear stress at 36 km depth is shown in Figure 15, and a cross-section is shown in Figure 16a. This assumes a strike, dip, and rake of 327°, 17°, and 90°, respectively, as representative of tremor source geometry on the transition zone of the northern Cascadia megathrust. The time-dependent stress on the subduction

interface (at that depth) would be the sum of the three displayed components. The stress changes are dominated by the elastic $\cos \omega t$ term, which attains a value of 0.11 kPa at the center of the circular load (and a maximum of 0.28 kPa at the edge). At the center, the net viscous component has an amplitude about 30% that of the elastic component. The combined elastic and viscous stress components lag 0.23 rad behind that of the forcing term (which has a $\cos \omega t$ time dependence). This is equivalent to a time delay of about 2 weeks between peak forcing and peak stressing below the center of the load.

4.3. Discontinuous Load

[25] The example of section 4.2 resembles the situation of the transition zone of the Cascadia subduction zone beneath Vancouver Island, the lateral extent roughly matching the geometry of loading of that region, which is truncated to the west by the ocean. In order to apply this analysis to the transition zone, it is necessary to consider the spatially
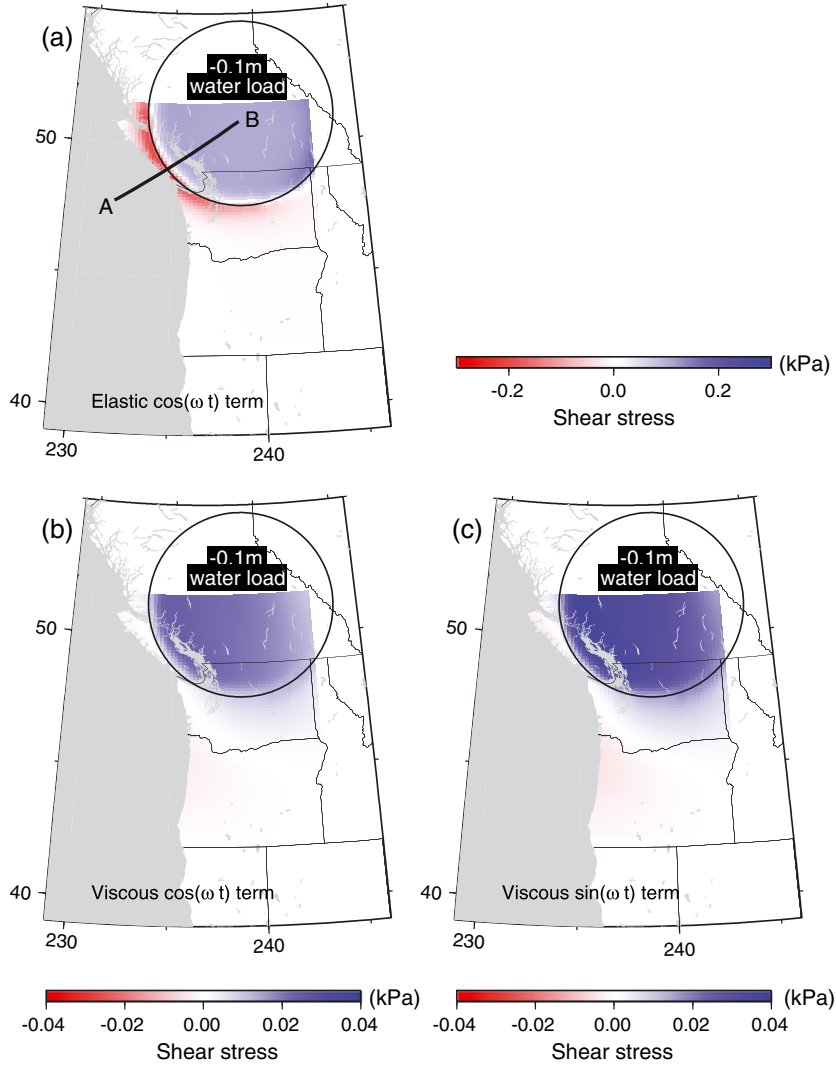
Figure 15. (a) Elastic $\cos \omega t$, (b) viscous $\cos \omega t$, and (c) viscous $\sin \omega t$ components of the viscoelastic response for annual loading of Earth's surface with an equivalent 10 cm water load over the indicated region. Downdip shear stress along a plane representing the transition zone of the northern Cascadia megathrust is evaluated at 36 km depth.

variable loading over a wider region and to exclude oceanic regions from such loading (the contribution of ocean tidal loading will be treated separately). The latter step is important because a discontinuous load produces a very different pattern of stress at depth. To illustrate this, we modify the continuous load over the circular region to be discontinuous, with the load absent at profile distances between 50 and 140 km from the southwestern edge of the circular region. This would correspond to an effective 50 km-wide loaded region on Vancouver Island and exclusion of the load over the Georgia Strait since it is connected with the ocean. Figure 16b shows the resulting elastic component of the downdip shear stress pattern at depth. Comparison with Figure 16a shows that the stress pattern at depths where tremor typically occur (25–55 km) are sensitive to relatively short-wavelength details of the load. Moreover, the downdip shear stress at greater depth ($\gtrsim$ 35 km) is predicted to be opposite to that at shallower depth ($\lesssim$ 35 km), i.e., 180° out of phase.

5. Annual Hydrological Cycle

[26] The water storage of the Pacific Northwest is constrained by GRACE satellite gravity observations, GLDAS integrated precipitation observations and land-surface modeling [*Rodell and Coauthors*, 2004], and absolute gravity measurements. We use GRACE and GLDAS solutions for the average monthly equivalent water thickness (EWT) in western North America on a regular grid with spacing of 0.5 degrees in both latitude and longitude. These are derived from processed GRACE gravity observations and GLDAS monthly water content summaries and extracted from online sources (http://grace.jpl.nasa.gov; http://grace.jpl.nasa.gov/data/gldas/). At each point on Earth's surface, the observed total water content (TWC) is modeled with three terms—a constant, a $\cos \omega t$, and a $\sin \omega t$ term:

$$\mathrm{TWC}(t_j) = \mathrm{constant} + A_1 \cos \omega t_j + A_2 \sin \omega t_j \quad (9)$$

where t_j is a monthly sample time and A_1 and A_2 are time-independent. We solve for A_1 and A_2 using 36 average
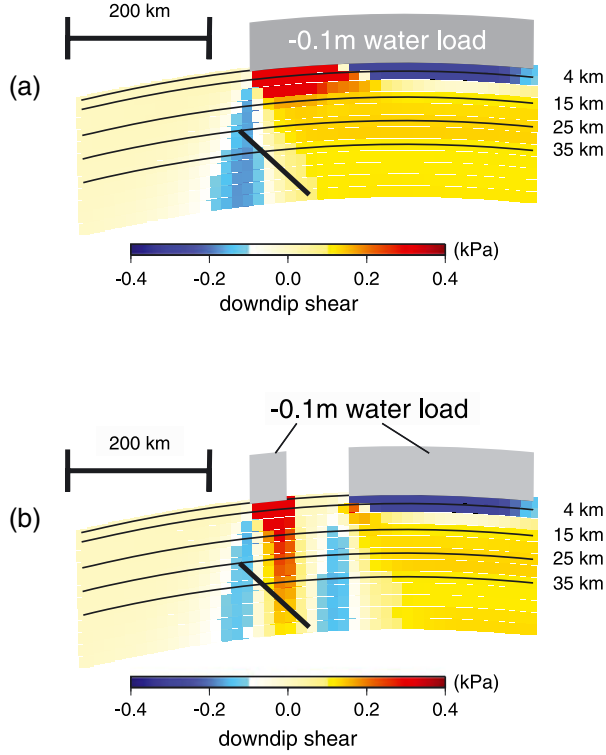
Figure 16. Vertical cross-section of downdip shear stress (Elastic $\cos \omega t$ term) through the southwestern edge of the circular load outlined in Figures 14 and 15. The profile location is shown in Figure 15. The profile strikes N57°E and passes through the center of the load. (a) Continuous load, identical to that considered in Figures 14 and 15. (b) Discontinuous load, with a 90 km-wide section removed. The transition zone from 25–55 km depth is indicated with the black line segment. Vertical exaggeration is a factor of 3.33.

monthly TWC over the time period 2006–2009 with a least squares fit, then rewrite equation (9) as

$$\text{TWC}(t_j) = \text{constant} + A \, \cos[\omega(t_j - t_0)] \tag{10}$$

where $A = \sqrt{A_1^2 + A_2^2}$ and $t_0 = (1/\omega)\tan^{-1}(A_2/A_1)$.

[27] Figure S2 shows the half-amplitude of annual equivalent water thickness A and time of the yearly maximum t_0 for both GRACE and GLDAS. For both data sets, the yearly maximum on Vancouver Island is generally achieved about 0.22 years into the year (i.e., mid-March). However, the GLDAS amplitude is substantially lower than that of GRACE, likely because GLDAS accounts for surface fluxes associated with soil moisture and snow load, whereas GRACE effectively measures the total water content in a vertical column that includes groundwater.

[28] Time-dependent GRACE gravity anomalies in southern Vancouver Island agree roughly with local absolute gravity measurements from 2002 to 2007 [*Lambert et al.*, 2007]. Both show a strong annual signal with maximum and minimum around mid-winter and mid-summer, respectively, with peak-to-peak variation of $\sim 6\mu$ Gal. This is equivalent to the emplacement of an infinite slab of water (on top of the crust in a non-porous volume) of peak thickness

15 cm in mid-winter and diminishing to zero in mid-summer, which is consistent with the derived water-storage amplitude $A \sim 7.5$ cm in southern Vancouver Island (Figure S2). The phase of the absolute gravity measurements, however, is advanced on average ~ 0.1 year ahead of GRACE; the absolute gravity measurements achieve a minimum ~ 0.62 years into the year, and the corresponding GRACE gravity minimum is achieved at 0.72 years. As the *Lambert et al.* [2007] measurements represent local storage conditions, we adopt a minimum water storage time of 0.62 years into the year in subsequent calculations.

6. Earth Ocean Tide Loading and Atmospheric Loading

[29] We estimate the load contributed by the annual Earth ocean tide with regional tide gauge data. Figure S3 shows the record of water level height at tide gauge stations in Tofino, Bamfield, and Victoria (Figure 1a) from 2000 to 2011. For each station, the superimposed curve shows a fit to the water level (WL) of the form

$$\text{WL}(t_j) = B_1 + B_2 t_j + B_3 \cos \omega t_j + B_4 \sin \omega t_j \tag{11}$$

With time measured from the beginning of the year, the best-fitting parameters for Tofino are $B_3 = 12.3$ and $B_4 = 1.0$ cm. The maximum load contributed by the ocean tide thus has peak-to-peak variations of about 25 cm and is, on average, maximal at about 0.01 year (3.6 days, i.e., early January) into every calendar year. This estimate does not account for the inverse barometer effect, which modifies sea level through atmospheric pressure fluctuations and tends to amplify sea level rise in areas where atmospheric pressure P_{atm} tends to be lower in winter months [e.g., *Wunsch and Stammer*, 1997]. Specifically, measured WL is

$$\text{WL}(t) = h_{\oplus}(t) - \frac{1}{\rho_w g}\text{P}_{\text{atm}}(t) \tag{12}$$

where $h_{\oplus}$ are the fluctuations of Earth ocean tides, ρ_w is water density, and g is the gravitational acceleration.

[30] To account for atmospheric pressure fluctuations in addition to Earth ocean tide fluctuations and on-land precipitation loads, we consider the atmospheric pressure applied to the ocean bottom and land surface. The ocean bottom pressure (OBP) and on-land pressure (LP) arising from combined time-dependent on-land precipitation, Earth ocean tides, and atmospheric pressure are

$$\text{OBP}(t) = \rho_w g \, \text{WL}(t) + \text{P}_{\text{atm}}(t)$$
$$\text{LP}(t) = \rho_w g \, \text{TWC}(t) + \text{P}_{\text{atm}}(t) \tag{13}$$

The addition of P_{atm} to OBP is equivalent to the inverse barometer correction. Note that the same amount of pressure must be applied to the land surface as well.

[31] Atmospheric pressure time series at six sites from 1987 to 2008 are shown in Figure S4. The best-fitting curve to these time series containing annual and semi-annual terms, i.e., of the form

$$\text{P}_{\text{atm}}(t) = C_1 + C_2 \cos \omega t + C_3 \sin \omega t + C_4 \cos 2\omega t + C_5 \sin 2\omega t \tag{14}$$

are also plotted in Figure S4, with corresponding values of peak-to-peak variation over the year listed. The largest such

11

annual variation is achieved at Tofino, equal to 3.1 mbar (= 0.31 kPa) with a minimum at 0.04 year into the year. To estimate the maximum impact of atmospheric pressure variations on shear stress at depth, we impose a load of 3.1 mbar on the combined ocean bottom and land surface, approximated as a uniform load on the entire surface of the spherical Earth, and evaluate the resulting downdip shear stress at depth. We find that the calculated downdip shear stress is about $0.05 - 0.10 \times P_{atm}$ (Figure S5), amounting to peak-to-peak variations of 0.016 to 0.032 kPa. This is much smaller than the downdip shear stress produced by either the land precipitation load or the uncorrected tidal load (i.e., $\rho_w g$ WL), and we henceforth neglect it.

7. Stress From Seasonal Loading

[32] Based on the simple example presented in section 3.2, it is clear that ± 10 cm water-equivalent mass changes can produce downdip stress changes on the order of 0.1–1 kPa. Such mass variations are realized over much of the Pacific Northwest. According to the absolute gravity measurements of *Lambert et al.* [2007], the epoch of maximum and minimum water storage is $\sim$ 0.12 and 0.62 years into the year, respectively. It is convenient to use the time of minimum water storage as the time of zero phase of the $\cos \omega t$ function used to prescribe the periodic loading (i.e., equation (5)). Hence the reference time of loading from the land sources is 0.62 years into each year.

[33] Using equation (13), we calculate the response of the viscoelastic Earth to the following: (1) the annual precipitation load on land and (2) the annual tide level. We first calculate the response to the on-land mass variations, prescribed by the equivalent water thickness TWC(t) in Figure S2, and convert the deformation to downdip shear stress at the time of minimum water storage along a SW-NE profile. The elastic $\cos \omega t$ component of this response is shown in Figure 17a. The stress contributed by the hydrologic load on land is about 0.2 kPa on most of the subduction interface.

[34] We next consider the load contributed by the annual Earth ocean tide as prescribed by the observed water level WL(t) extrapolated to the oceanic region covering the area 44 to 54°N, 132 to 120°W. The times of maximum and minimum tidal load are about 0.01 and 0.51 year into every year (Figure S3). This is advanced about 0.2 years ahead of the hydrologic load on land (Figure S2b). The downdip stress at the time of minimum tidal loading is shown in Figure 17b. The stress contribution on the subduction interface itself varies from 0 to 0.4 kPa, the larger values being achieved at shallower levels (depth $\lesssim$ 35 km).

[35] The superposition of stress from land and ocean loads still has an annual periodicity, but it involves a spatially variable combination of both, so that the phase of maximum stress from the combination will be spatially variable. The contributing components to these time series, i.e., from on-land precipitation (elastic and viscoelastic responses) and uncorrected ocean tides, are shown in Figure S6. At depth 45 km along the profile, approximately the deeper range where tremor occurs, the net maximum stress is achieved 0.66 years into the year. Time series of stress at this point are superimposed on Figure 9. The peak stress encouraging thrust motion—achieved when water storage is at a
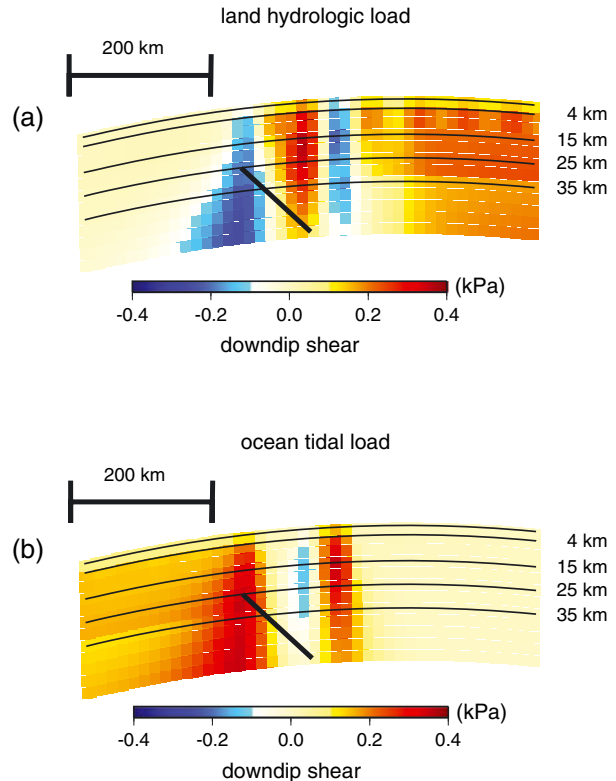

Figure 17. (a) Vertical cross-section of downdip shear stress (Elastic $\cos \omega t$ term) generated by the land hydrologic load (Figure S2a), where t is measured positive from a reference time 0.62 yr into the year) along a SW-NE profile (location shown in Figure 15). The transition zone from 25–55 km depth is indicated with the black line segment. (b) Downdip shear stress pattern produced by the annual ocean tide load (Elastic $\cos \omega t$ term, where t is measured positive from a reference time 0.51 year into the year). In both figures, vertical exaggeration is a factor of 3.33.

minimum in mid-summer—is correlated with the peak in NVT activity during the third quarter of the year (Figure 9).

8. Discussion

[36] The NVT detection algorithm that forms the basis of the Wech data set has quality criteria based on the uncertainty in tremor location [*Wech and Creager*, 2008], and this uncertainty depends on the background noise level. Some seasonal bias in tremor identification may exist because of systematically variable noise conditions over the year (the winter months likely being noisier), but the level of this bias is difficult to ascertain. In the Wech catalog, this bias can be partially judged by the number of stations contributing to detected seismic events in the NW and BC catalogs (Figure S1b and S1c). This month-by-month variability suggests that event detectability is not substantially worse in winter months than in summer months. In the Kao catalog, some guidance on the noise level which may affect seismic detection is provided by the "brightness" measure defined by equation (2) of *Kao and Shan* [2007]. This measure represents a sum of signals on contributing seismic stations, which arrive at the times expected for an assumed trial
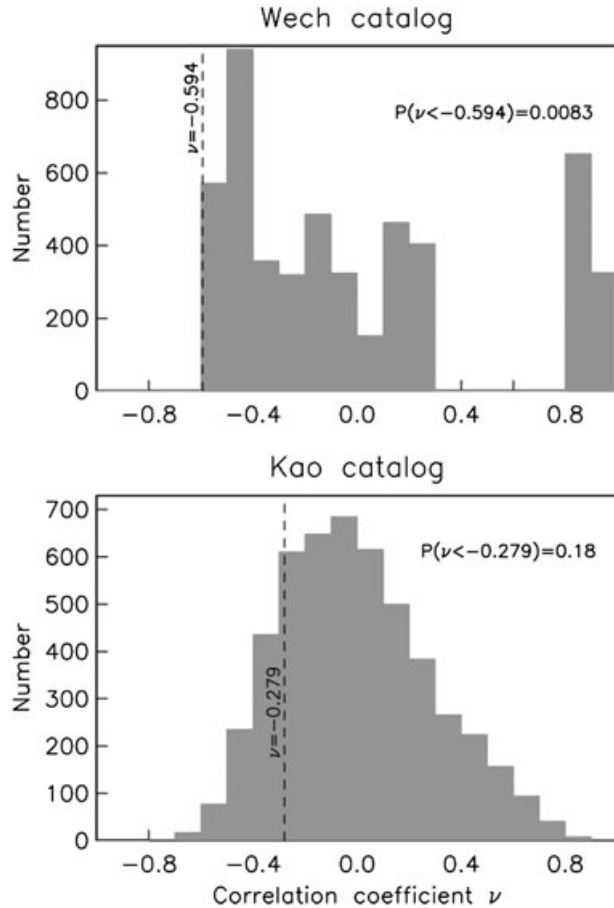
Figure 18. Histograms of correlation coefficient ν between number of ETS sub-events and precipitation in the preceding 2 months, obtained from 5000 realizations of shuffling the occurrence times of ETS in the (a) Wech catalog or (b) Kao catalog.

tremor hypocenter location. Lower values would result from relatively few contributing seismic stations but could also result from weaker seismic moment of the source itself. The brightness of tremor events in southern Vancouver Island does not vary significantly with time of year (Figure S7), suggesting that there is little bias in detectability of tremor events with respect to the time of year the event occurs.

[37] The statistical significance of the correlation between precipitation and tremor activity is quantified by further examining the first-order correlation between number of sub-events in ETS and the precipitation in the 2 months prior to that ETS; Figure 11 indicates an inverse correlation between the number of ETS sub-events and precipitation. Quantitatively, the correlation coefficient ν using the Wech and Kao catalogs is –0.594 and –0.279, respectively. To assess the statistical significance of these correlations, we perform Monte Carlo simulations in which the times of ETS are randomly shuffled among the times that they actually occurred, i.e., the precipitation information is preserved, but the number of ETS sub-events assigned to a particular time is resampled from the five (Wech catalog) or 13 (Kao catalog) ETS which actually occurred. In any one realization of this process, each ETS event still occurs exactly once but generally not at its original time. We perform 5000 realizations

for each of the Wech and Kao catalogs. Figure 18 demonstrates that most outcomes of this reshuffling do not yield such strong inverse correlations as the actual catalogs, i.e., most realizations yield higher ν than the observed ν-values indicated by the vertical dashed lines in the figure. We find that only 0.83% of the simulated ν-values are lower than –0.594 for the Wech catalog (i.e., only one out of 120 possible reshufflings of the five ETS times yields a smaller ν), and 18% of the simulated ν-values are lower than –0.279 for the Kao catalog. The fact that this fraction is not even lower for the Kao catalog reflects the fact that a few ETS (those that occurred in 1998, 1999, 2009, and 2011) were not especially strong even though they were preceded by little precipitation (Figure 11). An estimate of the significance of the correlation between precipitation and tremor activity is thus 82%.

[38] Figures 16 and 17 suggest that stress perturbations of order 1 kPa have a tangible effect on tremor activity. The peak downdip shear stress is achieved about 0.66 years into the year according to our model, which is dominated by the elastic stresses transmitted instantaneously by the surface load to depth (Figures S2b and 16b). The fact that seismicity tends to peak in the month of August (Figure 8) indicates at most a short (< 1 month) time lag between the surface loading and seismicity. This is consistent with the findings from other studies of seasonally correlated earthquakes in non-volcanic settings such as the Himalaya or the locked section of the San Andreas fault in Central California [*Bettinelli et al.*, 2008; *Christiansen et al.*, 2007], suggesting that elastic stress transmitted by the surface load is the dominant factor. It contrasts with the 1–6 month time lags between load and seismicity maxima in several volcanic areas in the western US [*Christiansen et al.*, 2005]. This may reflect the dominance of other processes in volcanic settings, particularly those related to fluid flow between Earth's surface and the shallow source volumes of highly cracked and permeable crust, which are superimposed on a relatively weak perturbation from the surface load itself.

[39] The largest clusters of events occurring in southern Vancouver Island involve both episodic tremor and episodic slip detected by geodesy, i.e., ETS. Figures 3 and 6 in the 1000 to 1100 km range of along-strike distance exhibit the quasi-14 month periodicity of ETS noted by numerous previous investigations [e.g., *Gomberg and the Cascadia 2007 and Beyond Working Group*, 2010]. Their regular occurrence and geodetically inferred slip associated with these events suggest that they are driven by tectonic processes of strain accumulation and release associated with the descent of the Juan de Fuca slab. These events show a strong tendency to occur in the third quarter of the year when the signal from hydrologic loading is maximized, as shown by the Figures 9 and 11. The much-smaller inter-ETS events are generally not detectable with geodetic data, although one such tremor burst has been detected with strainmeter data [*Wang et al.*, 2008]. We have evaluated the pattern of inter-ETS event occurrence by counting tremor events with ETS time periods excluded. The resulting event counts are slightly peaked in the second quarter of the year using both the Wech and Kao catalogs. This indicates that event clusters, when they do occur in the third quarter, tend to be much larger (i.e., ETS) than those clusters that occur in other quarters.

[40] Analysis of a 28 year tremor catalog (Herb Dragert, pers. comm.; catalog compiled by Garry Rogers and Herb

Dragert) confirms that ETS tend to occur in the third quarter of the year. The catalog covers the period 1982–2010 and reveals that 36% of ETS occur during the third quarter, significantly greater than the 25% expected by chance. The occurrence of a recent ETS in September 2012 (http://www.pnsn.org/tremor/ets-event-of-summer-2012), which appears strongest over central and southern Vancouver Island, is consistent with this pattern and our model of hydrological forcing.

[41] We have examined tremor activity in other distance ranges along the Cascadia subduction zone, i.e., outside the 1000–1100 km along-strike distance that is the focus of this study (Figure 4). Figures S8 and S9 show the spatial pattern of tremor from central Washington to northern Vancouver Island by quarter of the year using the 2006–2012 Wech and 1997–2011 Kao catalogs, respectively. Figures S10 and S11 show the corresponding tremor counts within the 900–1000 and 1100–1200 km along-strike distance ranges, i.e., northern Washington and central-northern Vancouver Island. We find a similar peak in the third quarter tremor activity using the 2006–2012 Wech catalog in northern Washington (Figures S8 and S10). This peak is weaker than that in southern Vancouver Island (Figure 8), and it is difficult to judge its significance since the Kao catalog adds little information further south. In central and northern Vancouver Island where the Kao catalog has very good sensitivity (and the Wech catalog has almost none), tremor occurrence is almost uniform throughout the year (Figures S9 and S11). The apparent lack of any seasonal component further north could be attributed to the narrowing of the Georgia Strait, so that the island land mass is effectively continuous with the mainland and will consequently have an unfavorable geometry for promoting downdip shear (Figure 16a).

[42] We have assumed that frictional resistance to slip on the deeper slab interface beneath southern Vancouver Island is negligible because of its sensitivity to small stress perturbations. However, it is also possible that rate-state friction effects may account for the apparent frequency-dependent slip behavior in subduction zones and elsewhere [*Lowry*, 2006]. This could permit parts of the Cascadia subduction zone to produce ETS in response to an annual load cycle and/or the diurnal tidal load cycle [*Hawthorne and Rubin*, 2010], depending on local conditions.

9. Conclusions

[43] The annual hydrological cycle produces a stress perturbation in the transition zone beneath southern Vancouver Island such as to promote downdip shear stress during the time of minimum water storage, i.e., mid-summer. Using two catalogs of non-volcanic tremor in northern Cascadia spanning the period from 1997 to 2012, combined with an estimate of the annual water storage cycle based on GRACE data, we find that this is manifested in seismicity patterns in two principal ways: (1) tremor events tend to occur in the third quarter of the year, when predicted downdip shear stress peaks and (2) the size of ETS sequences, as measured by the number of individual tremor bursts occurring during these sequences, is strongly correlated with the hydrologic load in place at the time of the ETS sequence.

[44] Satellite-based (GRACE) gravity and absolute gravity measurements are consistent and imply peak-to-peak annual variations in water storage in southern Vancouver Island of about 15 cm. When the hydrologic load on land and ocean tidal load are combined, our viscoelastic modeling then yields a magnitude of the downdip stresses at depth within the transition zone of about 0.2 or 0.4 kPa peak-to-peak annual variation.

[45] Although the northern Cascadia hydrologic cycle appears well correlated with tremor events, conditions may not always be favorable for such a physical mechanism to operate, as suggested by Figure 16a. We speculate that annual modulation of episodic tremor by seasonal hydrologic loading may occur in the transition zone of many other major subduction zones where conditions are favorable, e.g., where a situation such as that represented by the discontinuous load (Figure 16b) applies. The presence or lack of a detectable annual signal in GPS data [*Lowry*, 2006; *Vergnolle et al.*, 2010] does not necessarily constrain the existence of such modulation for other subduction zones.

Appendix A: Harmonic Forcing of a Maxwell Viscoelastic Material

[46] Here we derive harmonic oscillations of a Maxwell viscoelastic material undergoing pure shear. The stress-strain relation is

$$\dot{\epsilon} = \frac{\dot{\sigma}}{2\mu} + \frac{\sigma}{2\eta} \tag{A1}$$

where ϵ and σ are shear strain and shear stress, respectively, μ is shear modulus, η is viscosity. and a dot denotes differentiation with respect to time. We seek solutions of the form

$$\epsilon = \cos \omega t, \ \ \sigma = A \cos \omega t + B \sin \omega t \tag{A2}$$

Substitution of equation (A2) into equation (A1) yields

$$-\omega \sin \omega t = \left(-\frac{A\omega}{2\mu} + \frac{B}{2\eta}\right) \sin \omega t + \left(\frac{B\omega}{2\mu} + \frac{A}{2\eta}\right) \cos \omega t \tag{A3}$$

The cosine and sine terms of equation (A3) must match, leading to two simultaneous equations for A and B:

$$-\omega = -\frac{A\omega}{2\mu} + \frac{B}{2\eta} \tag{A4}$$

$$0 = \frac{B\omega}{2\mu} + \frac{A}{2\eta} \tag{A5}$$

The solution is

$$A = \frac{2\mu\gamma^2}{1+\gamma^2}, \ \ B = -\frac{2\omega\eta}{1+\gamma^2} \tag{A6}$$

where $\gamma = \omega\eta/\mu$ is a dimensionless parameter. The solution (A2) for σ may then be written

$$\sigma = C \cos(\omega t + \xi), \ \ C = 2\mu \frac{\gamma}{\sqrt{1+\gamma^2}}, \ \ \xi = \tan^{-1}(1/\gamma) \tag{A7}$$

[47] Figure A1 shows the normalized amplitude $C/2\mu = \gamma/\sqrt{1+\gamma^2}$ and phase ξ of σ. These represent the amplitude and phase shift of stress in the viscoelastic material relative to the equivalent elastic model. For high frequency ω or viscosity η, γ is large and the material behaves almost elastically.
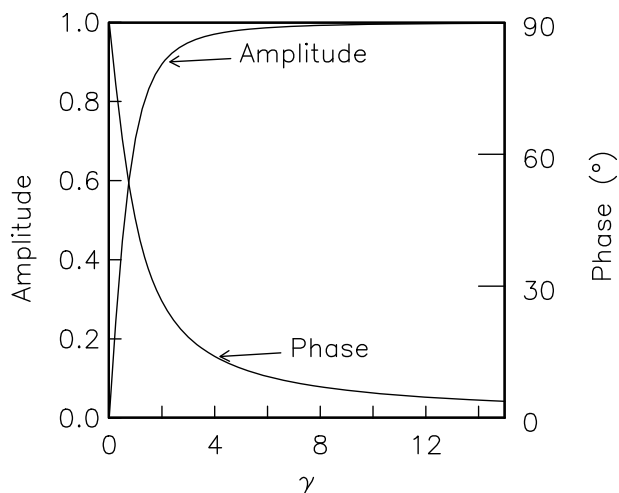
Figure A1. Amplitude and phase of σ as a function of γ.

References

Aguiar, A. C., T. I. Melbourne, and C. W. Scrivner (2009), Moment release rate of Cascadia non-volcanic tremor constrained by GPS, *J. Geophys. Res.*, *114*, B00A05, doi:10.1029/2008JB005,909.

Audet, P., M. G. Bostock, N. I. Christensen, and S. M. Peacock (2009), Seismic evidence for overpressured subducted oceanic crust and megathrust fault sealing, *Nature*, *457*, 76–78.

Audet, P., M. G. Bostock, D. C. Boyarko, M. R. Brudzinski, and R. M. Allen (2010), Slab morphology in the Cascadia forearc and its relation to episodic tremor and slip, *J. Geophys. Res.*, doi:10.1029/2008JB006053.

Bettinelli, P., J.-P. Avouac, M. Flouzat, L. Bollinger, G. Ramillien, S. Rajaure, and S. Sapkota (2008), Seasonal variations of seismicity and geodetic strain in the Himalaya induced by surface hydrology, *Earth Planet. Sci. Lett.*, *266*, 332–344.

Bollinger, L., F. Perrier, J.-P. Avouac, S. Sapkota, U. Gautam, and D. R. Tiwari (2007), Seasonal modulation of seismicity in the Himalaya of Nepal, *Geophys. Res. Lett.*, *34*, L08,304, doi:10.1029/2006GL029,192.

Bostock, M., A. Royer, E. Hearn, and S. M. Peacock (2012), Low frequency earthquakes below southern Vancouver Island, *Geochem. Geophys. Geosyst.*, doi:10.1029/2012GC004391.

Brudzinski, M. R., and R. M. Allen (2007), Segmentation in episodic tremor and slip all along Cascadia, *Geology*, *35*, 907–910.

Chapman, J. S., and T. I. Melbourne (2009), Future Cascadia megathrust rupture delineated by episodic tremor and slip, *Geophys. Res. Lett.*, *36*, L22,301, doi:10.1029/2009GL040,465.

Christiansen, L. B., S. Hurwitz, M. O. Saar, S. E. Ingebritsen, and P. A. Hsieh (2005), Seasonal seismicity at western United States volcanic centers, *Earth Planet. Sci. Lett.*, *240*, 307–321.

Christiansen, L. B., S. Hurwitz, and S. Ingebritsen (2007), Annual modulation of seismicity along the San Andreas Fault near Parkfield, CA, *Geophys. Res. Lett.*, *34*, L04,306, doi:10.1029/2006GL028,634.

Dragert, H., K. Wang, and T. S. James (2001), A silent slip event on the deeper Cascadia subduction interface, *Science*, *292*, 1525–1528.

Gomberg, J., and the Cascadia 2007 and Beyond Working Group (2010), Slow-slip phenomena in Cascadia from 2007 and beyond, *Geol. Soc. Am. Bull.*, *122*, 963–978.

Hawthorne, J. C., and A. M. Rubin (2010), Tidal modulation of slow slip in Cascadia, *J. Geophys. Res.*, *115*, B09,406, doi:10.1029/2010JB007,502.

Heki, K. (2001), Seasonal modulation of interseismic strain buildup in northeastern Japan driven by snow loads, *Science*, *293*, 89–92.

Heki, K., and T. Kataoka (2008), On the biannually repeating slow-slip events at the Ryukyu Trench, southwestern Japan, *J. Geophys. Res.*, *113*, B11,402, doi:10.1029/2008JB005,739.

Houston, H., B. G. Delbridge, A. G. Wech, and K. C. Creager (2011), Rapid tremor reversals in Cascadia generated by a weakened plate interface, *Nat. Geosci.*, *4*, 404–409.

Hu, Y., and K. Wang (2012), Spherical-Earth finite element model of short-term postseismic deformation following the 2004 Sumatra earthquake, *J. Geophys. Res.*, *117*, B05,404, doi:10.1029/2012JB009,153.

James, T. S., E. J. Gowan, I. Wada, and K. Wang (2009), Viscosity of the asthenosphere from glacial isostatic adjustment and subduction dynamics at the northern Cascadia subduction zone, British Columbia, Canada, *J. Geophys. Res.*, *114*, B04,405, doi:10.1029/2008JB006,077.

Kao, H., and S.-J. Shan (2007), Rapid identification of earthquake rupture plane using source-scanning algorithm, *Geophys. J. Int.*, *168*, 1011–1020.

Kao, H., S.-J. Shan, H. Dragert, and G. Rogers (2009), Northern Cascadia episodic tremor and slip: A decade of tremor observations from 1997 to 2007, *J. Geophys. Res.*, *114*, B00A12, doi:10.1029/2008JB006,046.

Lambert, A., J. Huang, N. Courtier, J. Liard, J. Henton, C. Klatt, and D. Winester (2007), Results from the GRACE prime mission: Monitoring water comparison of GRACE monthly estimates with surface gravity variations at North American sites, *Eos Trans. AGU*, Fall Meet. Suppl., abstract U21C–0626.

Lowry, A. R. (2006), Resonant slow fault slip in subduction zones forced by climatic load stress, *Nature*, *442*, 802–805.

McCausland, W., S. Malone, and D. Johnson (2005), Temporal and spatial occurrence of deep non-volcanic tremor: From Washington to northern California, *Geophys. Res. Lett.*, *32*, L24,311, doi:10.1029/2005GL024,349.

McCrory, P. A., J. L. Blair, D. H. Oppenheimer, and S. R. Walter (2006), Depth to the Juan de Fuca slab beneath the Cascadia subduction margin—A 3-D model for sorting earthquakes, *USGS Data Series, DS-91*, version 1.2.

Miller, M. M., T. Melbourne, D. J. Johnson, and W. Q. Sumner (2002), Periodic slow earthquakes from the Cascadia subduction zone, *Science*, *295*, 2423, doi:10.1126/science.1071,193.

Panet, I., F. Pollitz, V. Mikhailov, M. Diament, P. Banerjee, and K. Grijalva (2010), Upper mantle rheology from GRACE and GPS postseismic deformation after the 2004 Sumatra-Andaman earthquake, *Geochem. Geophys. Geosyst.*, *11*, Q06,008, doi:10.1029/2009GC002905.

Pollitz, F. F. (1996), Coseismic deformation from earthquake faulting on a layered spherical earth, *Geophys. J. Int.*, *125*, 1–14.

Pollitz, F. F. (1997), Gravitational viscoelastic postseismic relaxation on a layered spherical earth, *J. Geophys. Res.*, *102*, 17,921–17,941.

Pollitz, F. F. (2003), Transient rheology of the uppermost mantle beneath the Mojave Desert, California, *Earth Planet. Sci. Lett.*, *215*, 89–104.

Pollitz, F. F., P. Banerjee, and R. Bürgmann (2006), Postseismic relaxation following the great 2004 Sumatra-Andaman earthquake on a compressible self-gravitating Earth, *Geophys. J. Int.*, *167*, 397–420.

Rodell, M., and Coauthors (2004), The global land data assimilation system, *Bull. Am. Meteorol. Soc.*, *85*, 381394.

Rogers, G., and H. Dragert (2003), Episodic tremor and slip: The chatter of slow earthquakes, *Science*, *300*, 1942 1944.

Rubinstein, J. L., J. E. Vidale, J. Gomberg, P. Bodin, K. C. Creager, and S. D. Malone (2007), Non-volcanic tremor driven by large transient shear stresses, *Nature*, *448*, 579–582.

Rubinstein, J. L., M. LaRocca, J. E. Vidale, K. C. Creager, and A. G. Wech (2008), Tidal modulation of nonvolcanic tremor, *Science*, *319*, 186–189.

Shen, Z. K., Q. Wang, R. Bürgmann, Y. Wan, and J. Ning (2005), Pole-tide modulation of slow slip events at circum-Pacific subduction zones, *Bull. Seismol. Soc. Am.*, *95*, 2009–2015.

Vergnolle, M., A. Walpersdorf, V. Kostoglodov, P. Tregoning, and J. A. Santiago (2010), Slow slip events in Mexico revised from the processing of 11 year GPS observations, *J. Geophys. Res.*, *115*, B08,403, doi:10.1029/2009JB006,852.

Wang, K., H. Dragert, H. Kao, and E. Roeloffs (2008), Characterizing an 'uncharacteristic' ETS event in northern Cascadia, *J. Geophys. Res.*, *35*, L15,303, doi:10.1029/2008GL034,415.

Wang, K., Y. Hu, and J. He (2012), Deformation cycles of subduction earthquakes in a viscoelastic Earth, *Nature*, *484*, 327–332.

Wech, A. G. (2010), Interactive tremor monitoring, *Seismol. Res. Lett.*, *81*, 664–669.

Wech, A. G., and K. C. Creager (2008), Automated detection and location of Cascadia tremor, *Geophys. Res. Lett.*, *35*, L20,302, doi:10.1029/2008GL035,458.

Wech, A. G., K. C. Creager, and T. I. Melbourne (2009), Seismic and geodetic constraints on Cascadia slow-slip, *J. Geophys. Res.*, *114*, B10,316, doi:10.1029/2008JB006,090.

Wunsch, C., and D. Stammer (1997), Atmospheric loading and the oceanic inverted barometer effect, *Rev. Geophys.*, *35*, 79–107.